

Article

Preparation and Investigation of Micro-Transfer-Printable Single-Crystalline InP Coupons for Heterogeneous Integration of III-V on Si

Isabella Peracchi ¹, Carsten Richter ¹ , Tobias Schulz ¹, Jens Martin ¹, Albert Kwasniewski ¹, Sebastian Kläger ^{1,†} , Christiane Frank-Rotsch ¹, Patrick Steglich ²  and Karoline Stolze ^{1,*} 

¹ Leibniz-Institut für Kristallzüchtung (IKZ), 12489 Berlin, Germany

² IHP—Leibniz-Institut für Innovative Mikroelektronik, 15236 Frankfurt (Oder), Germany

* Correspondence: karoline.stolze@ikz-berlin.de

† Current address: LMU München, Department of Chemistry, Butenandtstr. 5-13, 81377 München, Germany.

Abstract: New requirements for high-frequency applications in wireless communication and sensor technologies need III-V compound semiconductors such as indium phosphide (InP) to complement silicon (Si)-based technologies. This study establishes the basis for a new approach to heterogeneous integration of III-V on Si aimed at the transfer of single-crystalline InP coupons on Si via micro-transfer printing (μ TP). The InP coupons will act as high-quality virtual substrates that allow selective homo-epitaxy. We present the chemical-mechanical polishing-based preparation and structural characterization of μ m-thin (001) InP platelets, starting from high-quality 4-inch bulk crystals and micro-patterning into transferable coupons of several hundred μ m². The obtained InP platelets exhibit the desired thickness—below 10 ± 1 μ m—and low surface roughness— <0.3 nm—on both sides, meeting the precondition for μ TP and epitaxy. X-ray rocking curve measurements provide accurate spatial maps of the total strain, which indicate small strain variations in the μ m-thin InP sample. Rocking curve mappings of the (0 0 4) reflection reveal half-widths below 16 arcsec in the majority of the sample area after thinning that is similar to commercially available InP bulk substrates. Pole figure measurements show no evidence of stress-induced micro-twinning or stacking faults. Overall, minor indications of crystal quality degradation in the product platelets, compared with the bulk samples, were detected.

Keywords: indium phosphide; compound semiconductor crystals; III-V on Si; CMP; X-ray diffraction; rocking curve imaging



Citation: Peracchi, I.; Richter, C.; Schulz, T.; Martin, J.; Kwasniewski, A.; Kläger, S.; Frank-Rotsch, C.; Steglich, P.; Stolze, K. Preparation and Investigation of Micro-Transfer-Printable Single-Crystalline InP Coupons for Heterogeneous Integration of III-V on Si. *Crystals* **2023**, *13*, 1126. <https://doi.org/10.3390/cryst13071126>

Academic Editor: Dmitri Donetski

Received: 23 June 2023

Revised: 7 July 2023

Accepted: 10 July 2023

Published: 19 July 2023



Copyright: © 2023 by the authors. Licensee MDPI, Basel, Switzerland. This article is an open access article distributed under the terms and conditions of the Creative Commons Attribution (CC BY) license (<https://creativecommons.org/licenses/by/4.0/>).

1. Introduction

The next generation of wireless communication technologies (6G) requires highly functional devices that use frequencies in the THz range for higher data rates and lower latencies while increasing energy efficiency, reliability and security [1–3]. These requirements exceed the physical limits of well-established complementary metal-oxide-semiconductor (CMOS) technologies based on silicon (Si). Hence, there is strong demand for other semiconductor materials with superior electronic and optical properties that complement Si. One of the key candidates is the III-V compound semiconductor, indium phosphide (InP). Due to their high electron mobility and high breakdown voltage, InP-based transistors allow access to frequencies well above 100 GHz [4,5]. Furthermore, its direct band gap enables light emission and detection of the respective InP-based devices in near infra-red regions, e.g., for free-space communication, optical fiber communication and optical interconnections between chips, especially at a wavelength of 1.55 μ m. Due to the favorable electronic and optical properties of InP, hetero-integration in Si-based CMOS technologies is particularly promising for electronic-photonics integrated circuits (EPIC) [6] in order to

extend the current functionalities with regard to nonlinear optical properties [7] and laser sources [8].

Existing approaches for integration of III-V on Si are facing major challenges regarding the structural quality of the III-V substrate or layers on one hand and process efficiency on the other: (i) Monolithic integration via direct hetero-epitaxial growth on Si leads to high threading and misfit dislocation densities (DD) due to the 8% lattice and thermal mismatch of InP and Si [9]. Different approaches to overcome the structural degradation did not reduce DD below 10^8 cm^{-2} in blanket InP layers [10–12]. Additionally, other defects, such as anti-phase boundaries, stacking faults and micro-twins, result from interface or growth effects, respectively. All these defects act as very efficient non-radiative recombination sites that dramatically degrade the final performance and reliability of the device. (ii) The flip-chip hybrid integration approach requires accurate alignment of the pre-fabricated chips; it is slow and limited with regard to integration density [13]. (iii) For wafer-to-wafer bonding, the difference in wafer diameter between commercially available Si (8–12 inches) and InP substrates (3–4 inches) leads to a high loss of Si material as well as expensive InP due to post-processing. Simultaneous integration of different III-V materials on a common substrate is also still challenging. Wafer-to-wafer bonding using direct bonding techniques requires high planarity, surface quality and thickness control for both Si and InP substrates and often results in low bonding yield [14]. Besides, a high annealing temperature leads to an increase in DD in the bonded InP substrate of more than two orders of magnitude, e.g., up to $6 \times 10^6 \text{ cm}^{-2}$ at 570 °C [15]. Another technique for wafer-to-wafer bonding is adhesive bonding using mainly benzocyclobutene (BCB). Its low thermal conductivity and optical absorption create high thermal resistance of bonded laser diodes and limit photonic integration. Furthermore, CMOS integration using BCB adhesive is not suitable for technological reasons [16]. (iv) In die-to-wafer bonding approaches, unprocessed III-V dies are bonded, with the epitaxial layers down, on processed Si wafers. This reduces material consumption compared with wafer-to-wafer bonding. However, for handling reasons, the die size cannot go below the mm range and thus limits integration density [13]. The problems associated with direct or adhesive bonding are the same as those described in the wafer-to-wafer case. For example, laser diodes bonded to Si via BCB between Si and the III-V epitaxial layer cannot operate in continuous-wave mode or at elevated temperatures due to the high thermal resistivity of the polymer [13].

A promising approach for III-V-on-Si is micro-transfer printing (μ TP), which involves the pickup and transfer of μm -sized chips, also called coupons, from a source substrate to a target substrate with high alignment accuracy using an elastomeric stamp [17]. The thickness of the coupons can range from sub-micrometer to 20 μm . The advantages of μ TP are high integration densities and efficient material use. The technique was previously implemented for III-V-on-Si photonic integrated circuits via the transfer of epitaxial III-V layers [18]. However, mechanical stress during the transfer process can destroy the sensitive epitaxial layer stacks and ultimately lead to device degradation. Additionally, a sacrificial interlayer used for release and a BCB adhesive used for bonding can lead to transfer issues and low operation temperatures, respectively, in the devices [16,19]. The coupons or devices could also be attached to the target substrate via direct van der Waals adhesion if the released surface is flat and smooth enough (typically root mean square roughness, $R_q \leq 1 \text{ nm}$). This adhesive-free situation would allow for potential electrical connections and improved heatsinking of the devices.

We pursue a new approach to hetero-integration of InP on Si aiming at low DD epitaxy templates, adhesive-free bonding for improved thermal conductivity, no need for growth of a sacrificial release layer and post-transfer epitaxy for conservation of sensitive layer stacks. This will be achieved by the transfer and bonding of single-crystalline InP coupons onto Si via μ TP. The InP coupons act as high-quality substrates for selective homo-epitaxy. If the high structural quality of the single-crystalline InP source material can be maintained, this process will provide templates for subsequent epitaxial growth with significantly lower DD compared with blanket InP layers hetero-epitaxially grown on Si. Using μ TP, the coupons

can be bonded on Si in a massively parallel manner precisely where they are needed for the device. In this way, it is possible to overcome the obstacles of the aforementioned approaches to hetero-integration of III-V on Si. A crucial step in this process is the coupon preparation. In this study, we present the preparation and structural characterization of μm -thin InP crystals as well as micro-patterning into transferable coupons.

2. Materials and Methods

2.1. Preparation of μm -Thin InP Crystals and InP Coupons

The S-doped 4-inch InP crystals with $1 \times 10^{18} \leq c_0(\text{Si}) \leq 4 \times 10^{18} \text{ cm}^{-3}$ and [001] growth direction used as high-quality single crystalline starting material were grown at IKZ with the vertical gradient freeze (VGF) technique. The KRISTMAG[®] technology was implemented for the simultaneous generation of heat and traveling magnetic field (TMF) in a heater-magnet module [20]. Further details of the growth process can be found in [21]. The as-grown crystals were sliced in a radial direction using a wire saw. For determination of the dislocation density of the initial bulk samples, wafer half-disks in [001] orientation were polished and defects were selectively etched with Huber's solution ($\text{HBr}:\text{H}_3\text{PO}_4 = 1:2$) [22]. Etch pits were counted on several spots in an area of approximately $(1.5 \times 1) \text{ mm}^2$ in $\langle 100 \rangle$ and $\langle 110 \rangle$ directions according to the DIN standard for etch pit density (EPD) analysis of InP [23,24]. A weighted mean value was calculated for each half-disk.

InP platelets with lateral dimensions of approximately $(11 \times 11) \text{ mm}^2$ and $(14 \times 14) \text{ mm}^2$ were sliced from the half-disks and glued to a plane-parallel glass support wafer with a polyethylenphthalat (PET)-based resin, Crystalbond 509 (PLANO), which forms a low-stress, thin fixing layer with $d \leq 2 \mu\text{m}$. The platelets were then chemical-mechanical polished (CMP) on one side to generate a planar, atomically flat surface. This side would later face downwards when bonding on the Si/SiO₂ wafer. After that, the InP platelets are removed from the glass wafer, glued back on the polished side facing the glass wafer, sanded down to $d \approx 150 \mu\text{m}$ and subsequently polished to the target thickness of $d \leq 10 \mu\text{m}$. The resin fixing layer serves as a sacrificial release layer later on in the process. CMP was performed with a PM5 and PM6 polisher/lapper from Logitech Ltd (Glasgow, UK). The polishing fluid used for coarse and fine polishing was Chemlox Polishing Fluid from Logitech Ltd. (pH = 12.2), which for thinning of the InP samples was supplemented with sodium hypochlorite (12% Cl, techn.), obtained from Carl Roth GmbH + Co. KG (Karlsruhe, Germany), to suppress uncontrolled etching (ratio 4:1, pH = 12.6). For end polishing, separate solutions of sodium hypochlorite (5% in water) and citric acid ($\geq 99.5\%$, p.a.; 10% in water), obtained from Carl Roth GmbH + Co. KG, were used. The felt-based polishing cloth for coarse polishing was a Suba[™] IV polishing pad and the polymer-based polishing cloth was an FP5 polishing pad (Pureon Inc., Willich, Germany). Material removal rates were determined by vision height measurements taken using a Quick Vision ELF measuring system (Mitutoyo, Neuss, Germany). Determination of the InP layer thickness was performed using IR-transmission data measured with a Lambda 1050 spectrophotometer (PerkinElmer, Rodgau, Germany) and fitting the interference signal from the two optical smooth InP surfaces to a transfer matrix model. This model contains the complex refractive index of InP in the wavelength range of 1000–2400 nm and the layer thickness as input parameters [25].

AFM measurements were carried out on a $(50 \times 50) \mu\text{m}^2$ sample area with a 384×384 mesh using a Dimension Icon AFM (Bruker, Billerica, MA, USA). Optical microscopy in differential interference contrast (Nikon Metrology GmbH, Düsseldorf, Germany) was performed using an Eclipse LV150N light microscope.

The thinned InP samples were patterned, producing a $1.4 \mu\text{m}$ mask of positive photoresist AZ ECI 3007 (Merck, Darmstadt, Germany) and optical lithography with a μMLA Maskless Aligner (Heidelberg Instruments, Heidelberg, Germany). The samples were then processed by wet etching in an $\text{HBr}:\text{H}_2\text{O}_2:\text{H}_2\text{O} = 10:1:50$ solution, which selectively dissolves the InP material. Step height measurements of samples at different etching stages were performed using a DektakXT[®] stylus profilometer (Bruker).

2.2. Structural and Opto-Electronic Characterization

A quantitative, lab-based X-ray diffraction (XRD) rocking curve imaging (RCI) was performed on one InP sample of (14×14) mm² before and after thinning with 800 μ m and 8(1) μ m sample thickness, respectively. Local rocking curves can be analyzed based on their width and position, revealing variations in strain and orientation. A Rigaku SmartLab high-resolution diffractometer equipped with a HyPix-3000 2D pixel detector was used to perform RCI with a spatial resolution at the 100- μ m level defined by the pixel size. The diffractometer uses a rotating anode and Cu $K\alpha_1$ radiation ($\lambda = 1.54059$ Å) selected by a 2-bounce Ge (004) Bartels monochromator. We recorded RCI data for the 0 0 4 Bragg reflections and three azimuthal positions (0° , 90° and 180°) to disentangle quantitative information about lattice tilt and lattice parameters. Details of the technique are described in [26]. For each point on the sample and the azimuthal positions, we determined the peak positions of the rocking scans as well as the integrated intensity and the peak FWHM. The true Bragg angle, and hence the c lattice parameter, can be determined by the average of the peak positions at $\varphi = 0^\circ$ and $\varphi = 180^\circ$. Accordingly, the difference equates to twice the local lattice tilt (pitch) of the normal of the lattice planes. The tilt in the perpendicular direction (roll) can be calculated from the average of the peak positions at $\varphi = 90^\circ$.

Pole figure measurements and $\omega/2\theta$ scans were performed using a GE XRD System XRD 3003 TT in Bragg-Brentano geometry with Cu $K\alpha_1$ radiation ($\lambda = 1.54059$ Å). To obtain information on the crystallographic phases present and the lattice orientation in the bulk and thinned InP sample, $\omega/2\theta$ scans were recorded for $10^\circ \leq 2\theta \leq 140^\circ$. XRD pole figures were collected at selected Bragg reflections to check for possible twins and stacking fault defects and to examine the corresponding crystal orientations before and after thinning.

Cathodoluminescence (CL) measurements/mappings were performed at RT using a Thermo Fisher Scientific Apreo S scanning electron microscope (SEM) equipped with a Gatan Monarc CL system. The utilized acceleration voltage was 5 kV utilizing a probe current of 1.6 nA. To detect a panchromatic signal, a photomultiplier was used. This allows for non-destructive detection and quantitative determination of dislocations in an 8(1) μ m-thin InP sample with a lateral dimension of (11×11) mm². For optoelectronic characterization of bulk and thinned InP samples, RT photoluminescence (PL) measurements were taken using a Horiba Jobin Yvon Raman spectrometer with a Si-CCD for detection and laser excitation at 633 nm.

3. Results and Discussion

3.1. Preparation and Characterization of μ m-Thin InP Crystals

For the transfer of single-crystalline InP epitaxy templates to Si, we developed a micro-preparation process [27] that starts from high-quality bulk single crystals with DD between 1×10^3 cm⁻² and 2×10^3 cm⁻² grown at IKZ, from which thinned InP platelets were prepared by sawing, grinding and optimized two-step CMP. Obtaining these μ m-thin InP crystals with two-sided polished, atomic smooth surfaces and low thickness variation demands delicate control of all relevant CMP parameters, including polishing solution, pressure, rotation speed, time, polishing cloth, fixing layer and pH value. Handling the crystals becomes especially challenging due to the mechanical properties of InP, a very soft and fragile material that easily forms cracks or cleaves along the {110} planes. The optimized two-step CMP process yielded InP platelets with the targeted thickness (Figure 1a). The abrasive-free final polishing step delivered samples with an excellent surface roughness of $R_q \approx 0.2$ nm for the back and front side of a (50×50) μ m² sample area based on AFM mappings (Figure 1b,c). This value meets the requirements for both adhesive-free bonding ($R_q \leq 1$ nm) and subsequent epitaxial growth ($R_q \leq 0.5$ nm). The AFM mapping of the back side is scratch-free, whereas only one shallow scratch is visible on the front side. The vertical curved lines in both maps correspond to the waviness ($W_q < 0.15$ nm) caused by the polishing process.

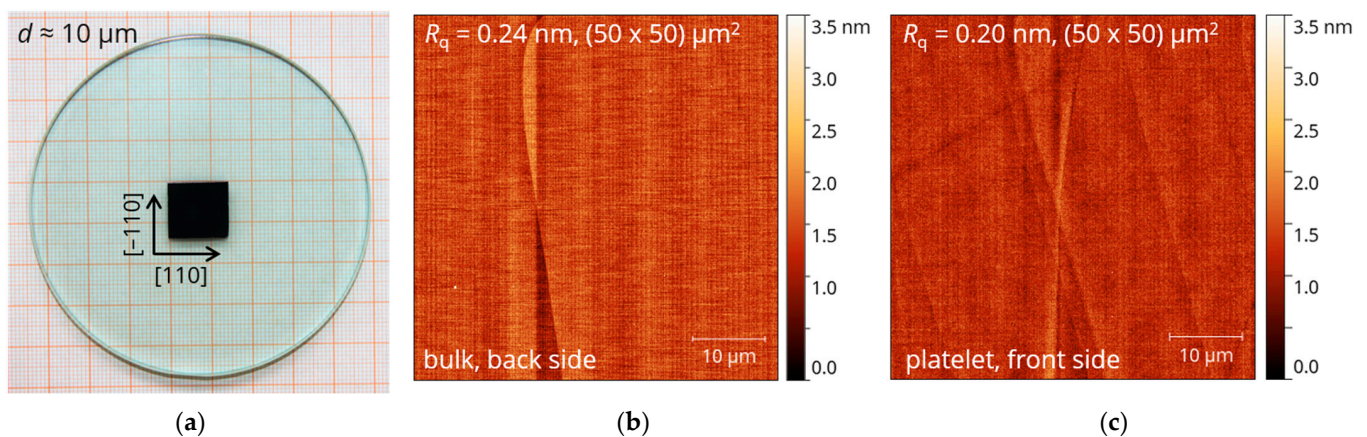


Figure 1. (a) Final thinned and polished InP platelet of $(14 \times 14) \text{ mm}^2$ mounted on a glass substrate. AFM scanning images of a $(50 \times 50) \mu\text{m}^2$ sample area of (b) back side bulk and (c) front side platelet surface after CMP with abrasive-free solutions.

The thickness of the InP layer is determined from IR transmission measurements. This method takes advantage of the interference fringes that occur when the light reflecting from the surface (air-platelet side) and interface (platelet-glass-substrate side) of a μm -thin platelet interferes with the light transmitted through it [28,29]. More information can be found in the supporting information. The results reveal an InP layer thickness of $\sim 8.5 \mu\text{m}$ (see Figure S1), which is below the targeted thickness of $10 \mu\text{m}$.

RCI provides accurate spatial maps of lattice deformations in the material that may be a consequence of mechanical processing. Maps of the rocking curve widths of the 004 reflection taken from a (001) InP sample before and after thinning are shown in Figure 2a. The images of the bulk sample were taken after the final polishing of the back side ($d = 800 \mu\text{m}$); the platelet images were collected from the same sample after flipping it upside down, grinding and end polishing. The FWHM map of the bulk sample shows a more homogeneous spatial distribution compared to the thinned platelet (Figure 2a). Small spherical spots of higher FWHM in the maps of the μm -thin sample indicate distorted areas. These can also be identified using optical microscopy, appearing as small craters in the DIC images (Figure S2), and are attributed to air bubbles trapped in the fixing layer. Areas of increased FWHM in the right upper and lower corner originate from high densities of trapped bubbles. The distortion represents a superposition of sample warpage from the air bubbles and possible lattice defects (strain and tilt), which cannot be distinguished based on the given RCI resolution. The local distortion can potentially be avoided in the future by sample fixation under increased vacuum. Nevertheless, the spatial distribution of the thinned platelet (Figure 2a) shows low RC widths for a major part of the sample. The histogram in Figure 2b reveals small FWHMs in the range of $14\text{--}18$ arcsec, marginally broader than the FWHM distribution of the bulk. Histogram peaks are at 14.6 arcsec and 15.6 arcsec for the bulk and thinned samples, respectively. These widths are narrow and similar to the FWHM (004) values of commercially available InP bulk substrates—e.g., 16 arcsec, 2-inch semi-insulating InP [30]. This reveals the high crystal quality before and after the thinning process. Edge effects, clearly visible in the increased FWHM maps of the thinned platelet, are of minor relevance for application.

Maps of total strain of the bulk sample (Figure 2c, left) show variations in strain on the mm scale that can also be observed as fringes in the FWHM maps in Figure 2a. We attribute these features to inhomogeneous adhesion to the glass substrate, leading to local bending of the InP bulk crystal (Figure S3), and slight variations in the lattice parameter. However, the strain features are not visible in the strain maps of the thinned sample (Figure 2c, right), indicating an elastic deformation that disappears once the stress is removed by releasing the bulk sample from the glass substrate.

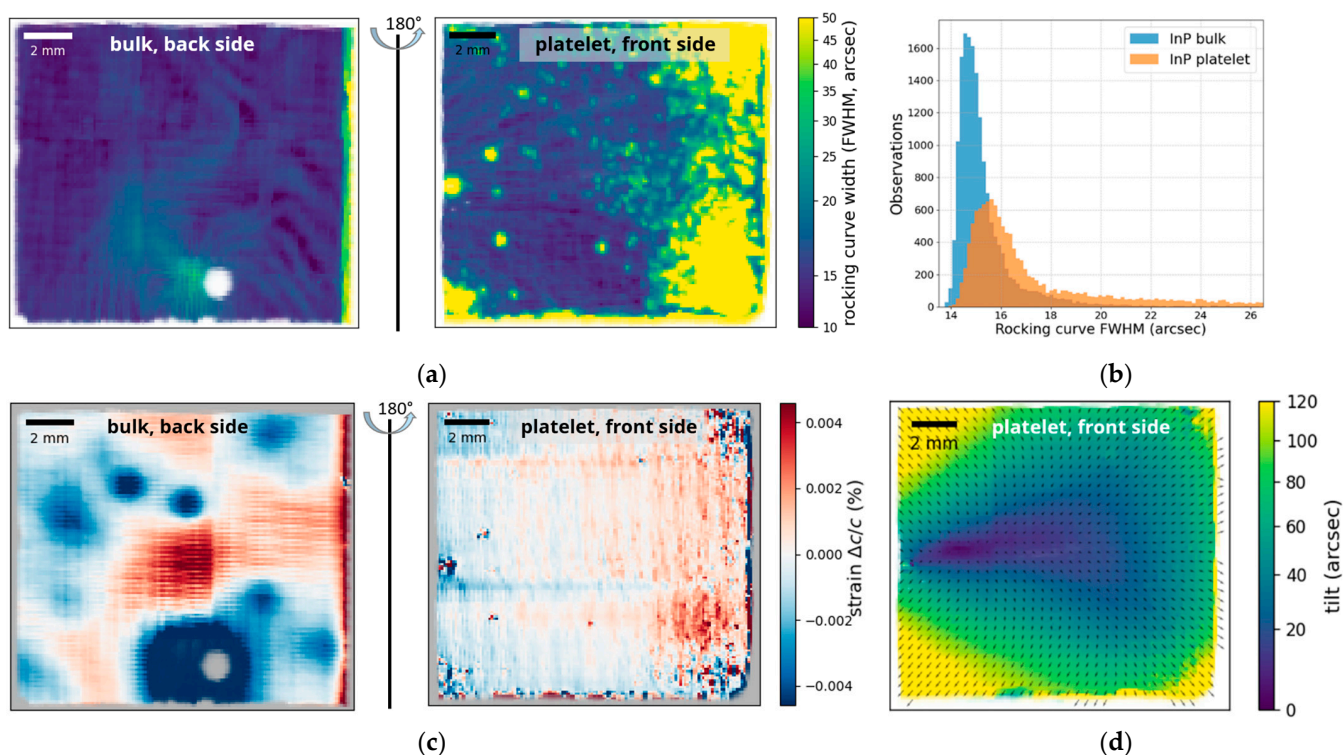


Figure 2. RCI data of the 0 0 4 reflection of the (001)-oriented InP samples: (a) FWHM maps before and after thinning (the sample was flipped during the process, the white dot-like indicates missing data due to a high local tilt that was not covered by the angular range of the rocking curve) and (b) FWHM histograms from (a). Calculated strain (c) before and after thinning (the sample was flipped during the process, the grey dot-like area indicates missing data) and (d) mapped tilt of (001) lattice planes for the sample after thinning.

The thinned platelet shows overall small strain variations in Figure 2c, right ($\pm 0.004\%$). The biggest differences in strain are visible on the right upper and lower corner and are caused by high densities of trapped air bubbles (see also Figure 2a, right). However, as the strain from inhomogeneous adhesion observed in the bulk sample is likely generated from elastic deformation, which disappears by releasing the sample from the substrate, the same can be expected of the strain from air bubbles in the thinned platelet. In the future, mechanical stress on the material can further be minimized early on in the thinning process by ensuring void-free fixing layers. Stitching effects are visible in the strain maps of both samples as parallel horizontal and vertical lines, respectively (the thinned sample was placed in the diffractometer rotated 90° compared to the bulk sample). The sample curvature was calculated from the linear slope of Bragg peak positions from different sample locations. The global curvature before and after thinning was approx. $\pm 0.0007^\circ/\text{mm}$ and $\pm 0.003^\circ/\text{mm}$, corresponding to curvature radii of $\pm 80\text{ m}$ and $\pm 20\text{ m}$, respectively. Although the curvature increases by a factor of approximately 4, the tilt mapping in Figure 2d shows no global waviness after thinning. Damage due to mechanical stress during CMP on such thin samples is only observed in small regions on the rim.

The X-ray $\omega/2\theta$ scan of the 001-oriented bulk and thinned InP sample in Figure 3a shows the presence of the (002), (004) and (006) zinc blende (ZB) Bragg reflections with high intensity and narrow widths, which occur at $2\theta = 30.30^\circ$, $2\theta = 63.22^\circ$ and $2\theta = 103.82^\circ$, respectively. They indicate the expected (001) orientation of the ZB-type phase with a vertical lattice parameter of $a = 5.8817\text{ \AA}$. Additional broad reflections of very low intensity occur in both scans at approximately $2\theta = 15.2^\circ$ and $2\theta = 47.3^\circ$ and can be attributed to the kinematically forbidden reflections 001 and 003 (violated reflection condition for $F\text{-}43m\text{ h}00: h = 2n$). The CMP thinning process does not affect the overall lattice orientation and crystallinity as the $\omega/2\theta$ scans before and after thinning are identical and the forbidden re-

flections are already present in the bulk sample. However, the weak 001 and 003 reflections suggest the existence of areas with atomic rearrangement that lead to symmetry-breaking. One possible reason may be surface reconstruction from dangling bonds in damaged atomic layers on the sample surface, which changes the Bravais lattice. Further investigations, which exceed the scope of this study, are needed for elucidation. Two additional narrow, low-intensity peaks marked with stars in the $\omega/2\theta$ scan at $2\theta = 27.29^\circ$ and $2\theta = 56.48^\circ$ in Figure 3a can be attributed to 002 and 004 reflections, respectively, generated with Cu $K\beta$ radiation ($\lambda = 1.39225 \text{ \AA}$).

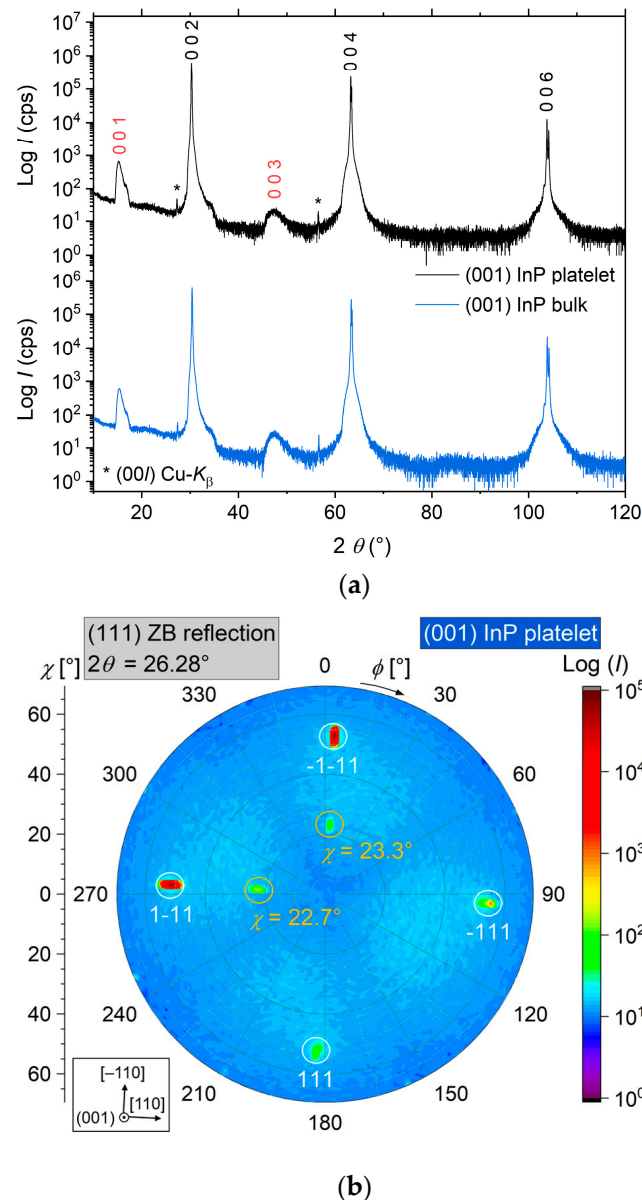


Figure 3. (a) X-ray $\omega/2\theta$ scan of the 001-oriented bulk and thinned InP sample, 002 and 004 reflections generated by Cu $K\beta$ radiation are indicated with *. (b) X-ray pole figure measured at $2\theta = 26.28^\circ$ of the thinned (001) InP platelet; the sample orientation is indicated. The intensity (cps) is plotted on a logarithmic scale.

In order to reveal twins and stacking faults, XRD pole figure measurements were performed for the (111) Bragg reflections of InP. Therefore, a series of full polar scans (χ) at different azimuthal angles (ϕ) obtained by setting the diffractometer at the fixed ω and 2θ values of the (111) reflection of InP was obtained. Figure 3b shows a pole figure taken using

the InP (111) ZB Bragg reflection condition ($2\theta_{111} = 26.28^\circ$). Strong peaks with four-fold symmetry can be found at a polar angle χ between 51.8° and 55.3° corresponding to the {111} InP reflections ($\chi = 54.75^\circ$, deviation due to tilt between sample surface normal and 001 lattice normal). The twinning operation in InP can be described as a lattice rotation by 180° around the $\langle 111 \rangle$ axis, thereby transforming the [001] growth direction into [22-1] in the twin. Similarly, twins can be explained as stacking faults in the $\langle 111 \rangle$ directions, where the cubic closest packed lattice (stacking frequency A–B–C) is interrupted by one hexagonal stack (A–B). Twinning or stacking faults in InP would generate additional InP (111) peaks observable in the central region of an InP (111) pole figure located at $\chi = 15.8^\circ$ and correspond to the angle between the {111} planes of InP in the twinned lamellas or to the stacking faults. No evidence of such cubic twin peaks was found in the pole figure around said polar angle in Figure 3b. Nevertheless, two additional diffraction peaks with low intensity at $\chi = 22.7^\circ$ and $\chi = 23.3^\circ$ align along the azimuths of the {111} InP reflections, which were also detected in the pole figure of the bulk sample (Figure S4). The polar angles of the weak peaks are in good agreement with the {113} InP reflections, although the observed 2θ value is approximately $2\theta_{113}/2$ ($2\theta_{113} = 51.61^\circ$). This topic is the subject of ongoing investigations, which are not within the scope of this study.

For most microelectronic and photonic devices, InP substrates with high structural quality of low DD are crucial. Dislocations introduce electronic states in the band gap of the III-V material system. These energy states have a strong electrical and optical impact on the device's performance. They can act as non-radiative recombination centers that generate phonons, which in turn can create even more defects through local heating, known as recombination-enhanced defect reaction. This leads to a reduction in photon emission efficiency [31] and/or minority carrier lifetime [32–34], as well as an increase in leakage current [35]. The lifetime of III-V lasers strongly decreases with increasing DD [36]. In order to prolong the lifetime of quantum well lasers with a typical footprint of $10\ \mu\text{m}$ of the active region, the mean inter-dislocation distance l must be $>10\ \mu\text{m}$, which corresponds to a maximum DD of $10^6\ \text{cm}^{-2}$ according to $l = \frac{1}{\sqrt{DD}}$. Therefore, in this study, we targeted DDs in the μm -InP crystals significantly lower than the critical value of $10^6\ \text{cm}^{-2}$, in order to obtain high-quality substrates for selective epitaxy.

For non-destructive determination of the DD and evaluation of potential sub-surface damage from CMP in thinned samples, we performed panchromatic CL measurements on a $10\text{-}\mu\text{m}$ InP sample. In the corresponding CL mapping (Figure 4), dislocations were revealed by locally reduced CL intensity in the form of dots or lines due to the fact that they serve as non-radiative recombination sites. The dark dots (marked with red circles) are caused by threading dislocations with a line direction parallel to the surface normal. Two black frames (Figure 4, frame 2 and 3) show examples of threading dislocations in more detail. A short, narrow line extending from the right corner framed in blue is aligned along the $\langle 110 \rangle$ direction, which is related to the glide geometry of the system. This glide band is depicted in more detail in a highlighted blue frame (1) of Figure 4. Similar lines oriented along the $\langle 110 \rangle$ direction were observed in CL images of an InP:S doped (100) sample [37]. Extended dark lines without any reference to the underlying crystal symmetry would indicate surface or subsurface scratches, which cannot be observed in our layers. The DD of the examined (200×200) μm^2 area amounts to approximately $7 \times 10^4\ \text{cm}^{-2}$ and is therefore higher than the EPD value from the corresponding bulk crystal wafer of $1.3 \times 10^3\ \text{cm}^{-2}$. Although, it is still well below our critical target value of $10^6\ \text{cm}^{-2}$. The increased DD in the thinned sample compared with the average EPD from DSE was not necessarily induced by the preparation process, but rather already existed in the bulk crystal. An inhomogeneous distribution of dislocations and a locally increased DD in the examined CL area of the platelet can lead to the discrepancy.

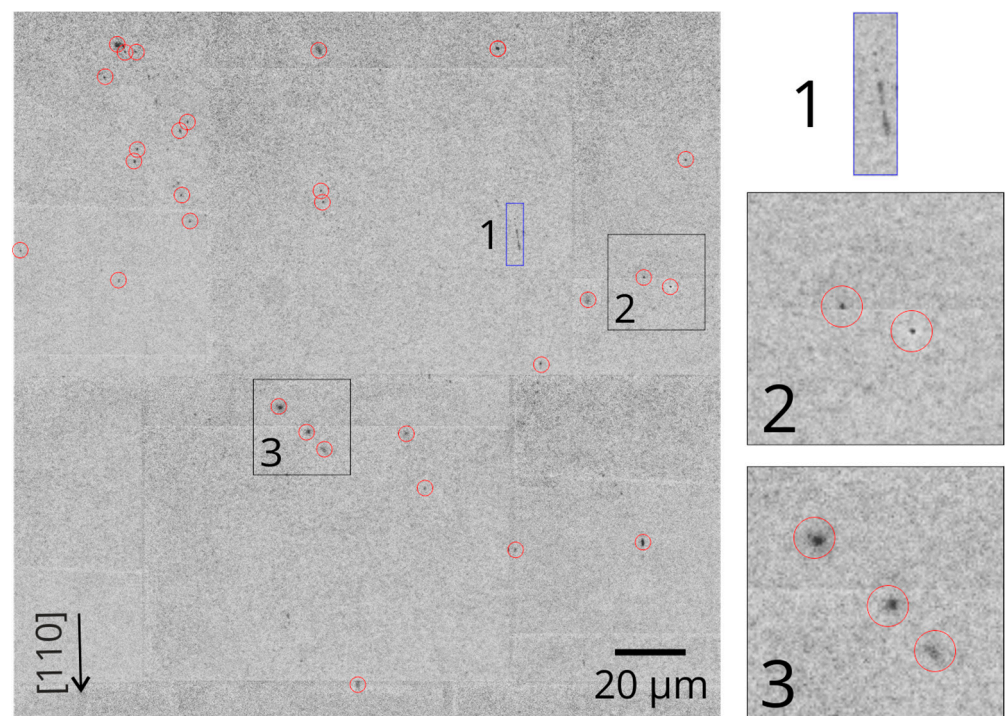


Figure 4. CL mapping of a (001) sample after thinning an area of $(200 \times 200) \mu\text{m}^2$, with framed regions of dark lines (1) and dark dots (2,3) shown in more detail; vertical and horizontal grey lines are artifacts from stitching.

Room-temperature PL measurements of polished bulk and thinned InP samples (see Figure S5) showed no significant difference in the luminescence spectra with maxima at 918 nm and 915 nm, respectively. The peak values correspond to the band edge emission of the room-temperature band gap of InP (1.35 eV).

3.2. Micro-Patterning of InP Coupons

In order to produce μm -sized transfer-printable coupons, the InP platelets were micro-structured using lithography-assisted patterning in conjunction with wet etching as depicted in the schematic illustration in Figure 5a, steps I–III. InP platelets could successfully be patterned to 100–400 μm -sized coupons, as shown in Figure 5b, with a low lateral undercut of $<5 \mu\text{m}$. For the transfer, the InP coupons need to be encapsulated with a photoresist with local openings to access the resin fixing layer, which is then selectively dissolved in an aprotic, polar solvent mixture, leaving the free-standing InP coupons anchored to the glass substrate by tethers as shown in Figure 5a, steps IV–V. Afterward, the coupons can be picked up with a stamp and transferred to the Si target wafer. The main innovation in this process is the PET resin which serves as a low-stress fixing layer for CMP as well as a sacrificial layer for later release. In contrast to selective under-etching of epitaxial grown sacrificial layers, e.g., InGaAs or InAlAs for InP-based structures, the solvent used for underetching the PET resin does not dissolve InP. Its selectivity is extremely high; therefore, the surface roughness and flatness of the back side of the InP samples are solely dependent on the CMP process and stay atomically flat in our case. For InGaAs/InP or InAlAs/InP layer systems and aqueous iron chloride etchant, the roughness increases with etch duration and results in high roughness of $2 \text{ nm} < R_q < 9 \text{ nm}$, unsuitable for van der Waals adhesion [16]. Furthermore, the $\text{FeCl}_3 \cdot \text{H}_2\text{O}$ solution causes Fe^{3+} contamination of the cleanroom process equipment and needs to be avoided.

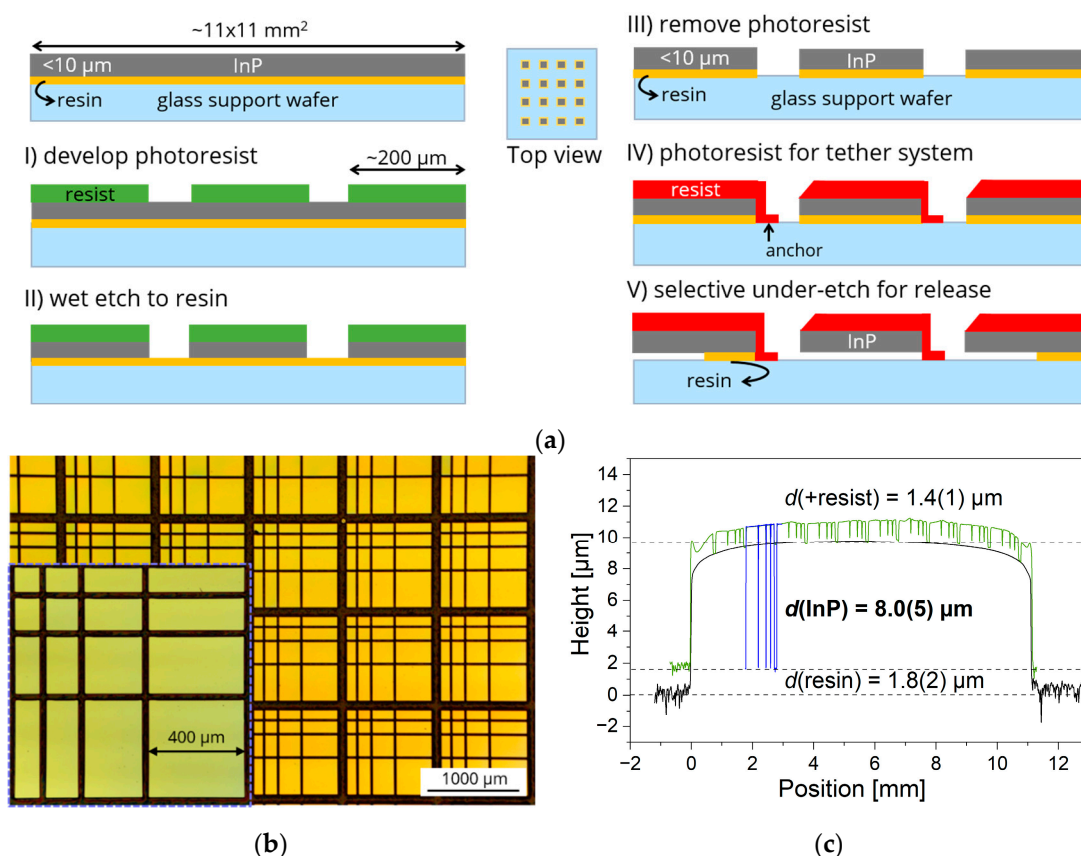


Figure 5. (a) Schematic illustration of the micro-patterning of transfer-printable single-crystalline InP coupons; (b) DIC microscopic image of etched InP coupons, with the inset showing more detail and (c) height profiles of $(11 \times 11) \text{ mm}^2$ InP platelet with resin (black), additional patterned resist according to step I (green) and after wet etching of the InP according to step II (blue).

Complementary to IR transmission measurements, the thickness of the InP sample can be determined using a stylus profilometer. Therefore, the total sample profile, which consists of the total height of the InP layer and the PET resin layer as well as the height of profiles from different micro-patterning process steps, i.e., the resist development step I and the wet etching step II, were measured (see Figure 5c). The differences between those profiles result in an InP sample thickness of $\sim 8.0 \mu\text{m}$ with low thickness deviation $< 1 \mu\text{m}$, in good agreement with the IR transmission data, as well as in a resin layer thickness of $\sim 2 \mu\text{m}$.

4. Conclusions

The presented study lays the basis for a new approach to hetero-integration of InP on Si. In summary, the feasibility of μm -thin InP platelet fabrication starting from VGF-grown bulk crystals was demonstrated. The development of this procedure was accompanied by precise defect monitoring. FWHM mappings from high-resolution XRD imaging of a thinned InP sample show low RC widths for major parts in the spatial distribution. Locally increased FWHM values originate from elastic deformation caused by inhomogeneous adhesion of the bulk and the μm -thin sample to the substrate and correspond to small strain variations in the total strain maps. For all applied XRD techniques, no signs of systematic crystal quality deterioration in the product platelets compared with bulk samples were detected and PL measurements on bulk and thinned InP samples show no significant difference in the respective luminescence spectra. The DD examined using CL is one order of magnitude higher than the EPD value from the corresponding bulk crystal but still well below our critical target value of 10^6 cm^{-2} .

The obtained InP platelets meet the structural prerequisites of (i) low and uniform thickness ($8 \pm 1 \mu\text{m}$) needed for μTP , (ii) low roughness on the back and front sides ($<0.3 \text{ nm}$) for adhesive-free bonding and epitaxy, as well as (iii) small FWHM ($<16 \text{ arcsec}$) and (iv) low DD ($\ll 10^6 \text{ cm}^{-2}$), both of which are required for high-quality epitaxy templates. Furthermore, (v) the InP platelets could successfully be patterned to 100–400 μm -sized coupons by employing photolithography and wet etching. With the present findings, we are able to take the next steps towards hetero-integration on Si via μTP . This new method will enable device layers with significantly reduced DD compared with hetero-epitaxial growth due to selective homo-epitaxy on the virtual InP substrates. In addition, improved thermal conductivity and the preservation of sensitive layer stacks through adhesive-free bonding and post-transfer epitaxy, respectively, will result in distinct advantages over existing bonding techniques.

5. Patents

German patent filed-DE 10 2022 100 661.1.

EU patent filed-EP 23 151 074.4.

Supplementary Materials: The following supporting information can be downloaded at <https://www.mdpi.com/article/10.3390/cryst13071126/s1>, Figure S1: IR transmission of a (001) InP platelet, Figure S2: Mapped rocking curve FWHM and DIC micrograph of a (001) InP platelet, Figure S3: Mapped lattice parameter of a (001) InP bulk sample, Figure S4: X-ray pole figure of a (001) InP bulk sample, Figure S5: PL spectra of (001) InP bulk and platelet sample. References [38,39] are cited in the supplementary materials.

Author Contributions: Conceptualization, I.P., P.S. and K.S.; methodology, K.S., C.R. and J.M.; software, I.P., C.R. and T.S.; formal analysis, A.K.; investigation, I.P., C.R., T.S., S.K. and K.S.; resources, C.F.-R.; data curation, K.S.; writing—original draft preparation, I.P. and K.S.; writing—review and editing, K.S., C.R., P.S. and J.M.; visualization, I.P., K.S. and C.R.; supervision, K.S. All authors have read and agreed to the published version of the manuscript.

Funding: This research received no external funding.

Data Availability Statement: Not applicable.

Acknowledgments: The authors thank Katrin Berger, Manuela Imming-Friedland and Thomas Wurche for their technical support, and Katrin Berger, Manuela Imming-Friedland and Uta Juda for their valuable discussion on CMP. The authors especially thank Robert Kernke for his support with taking measurements and stitching CL images, and Uta Juda for the EPD analysis.

Conflicts of Interest: The authors declare no conflict of interest.

References

1. Wikström, G.; Peisa, J.; Rugeland, P.; Johansson, N.; Parkvall, S.; Girnyk, M.; Mildh, G.; Silva, I.L.D. Challenges and Technologies for 6G. In Proceedings of the 2020 2nd 6G Wireless Summit (6G SUMMIT), Levi, Finland, 17–20 March 2020; pp. 1–5.
2. Alsharif, M.H.; Kelechi, A.H.; Albreem, M.A.; Chaudhry, S.A.; Zia, M.S.; Kim, S. Sixth Generation (6G) Wireless Networks: Vision, Research Activities, Challenges and Potential Solutions. *Symmetry* **2020**, *12*, 676. [CrossRef]
3. Amakawa, S.; Aslam, Z.; Buckwater, J.; Caputo, S.; Chaoub, A.; Chen, Y.; Corre, Y.; Fujishima, M.; Ganghua, Y.; Gao, S.; et al. *White Paper on RF Enabling 6G—Opportunities and Challenges from Technology to Spectrum*; University of Oulu: Oulu, Finland, 2021; ISSN 2669-963X.
4. Rode, J.C.; Chiang, H.-W.; Choudhary, P.; Jain, V.; Thibeault, B.J.; Mitchell, W.J.; Rodwell, M.J.W.; Urteaga, M.; Loubychev, D.; Snyder, A.; et al. Indium Phosphide Heterobipolar Transistor Technology Beyond 1-THz Bandwidth. *IEEE Trans. Electron Devices* **2015**, *62*, 2779–2785. [CrossRef]
5. Urteaga, M.; Griffith, Z.; Seo, M.; Hacker, J.; Rodwell, M.J.W. InP HBT Technologies for THz Integrated Circuits. *Proc. IEEE* **2017**, *105*, 1051–1067. [CrossRef]
6. Mai, A.; Steglich, P.; Mai, C.; Simon, S.; Scholz, R. Electronic-Photonic Wafer-Level Technologies for Fast Prototyping and Application Specific Solutions. In Proceedings of the 2019 Photonics Electromagnetics Research Symposium—Spring (PIERS-Spring), Rome, Italy, 17–20 June 2019; pp. 249–255.
7. Jiao, Y.; van der Tol, J.; Pogoretskii, V.; van Engelen, J.; Kashi, A.A.; Reniers, S.; Wang, Y.; Zhao, X.; Yao, W.; Liu, T.; et al. Indium Phosphide Membrane Nanophotonic Integrated Circuits on Silicon. *Phys. Status Solidi (A)* **2020**, *217*, 1900606. [CrossRef]

8. Tran, M.A.; Huang, D.; Guo, J.; Komljenovic, T.; Morton, P.A.; Bowers, J.E. Ring-Resonator Based Widely-Tunable Narrow-Linewidth Si/InP Integrated Lasers. *IEEE J. Sel. Top. Quantum Electron.* **2020**, *26*, 1500514. [[CrossRef](#)]
9. Li, Q.; Lau, K.M. Epitaxial Growth of Highly Mismatched III-V Materials on (001) Silicon for Electronics and Optoelectronics. *Prog. Cryst. Growth Charact. Mater.* **2017**, *63*, 105–120. [[CrossRef](#)]
10. Kunert, B.; Mols, Y.; Baryshnikova, M.; Waldron, N.; Schulze, A.; Langer, R. How to Control Defect Formation in Monolithic III/V Hetero-Epitaxy on (100) Si? A Critical Review on Current Approaches. *Semicond. Sci. Technol.* **2018**, *33*, 093002. [[CrossRef](#)]
11. Shi, B.; Klamkin, J. Defect Engineering for High Quality InP Epitaxially Grown on On-Axis (001) Si. *J. Appl. Phys.* **2020**, *127*, 033102. [[CrossRef](#)]
12. Han, Y.; Yan, Z.; Xue, Y.; Lau, K.M. Micrometer-Scale InP Selectively Grown on SOI for Fully Integrated Si-Photonics. *Appl. Phys. Lett.* **2020**, *117*, 052102. [[CrossRef](#)]
13. Roelkens, G.; Van Campenhout, J.; Brouckaert, J.; Van Thourhout, D.; Baets, R.; Romeo, P.R.; Regreny, P.; Kazmierczak, A.; Seassal, C.; Letartre, X.; et al. III-V/Si Photonics by Die-to-Wafer Bonding. *Mater. Today* **2007**, *10*, 36–43. [[CrossRef](#)]
14. Guo, X.; He, A.; Su, Y. Recent Advances of Heterogeneously Integrated III–V Laser on Si. *J. Semicond.* **2019**, *40*, 101304. [[CrossRef](#)]
15. Pasquariello, D.; Camacho, M.; Ericsson, F.; Hjort, K. Crystalline Defects in InP-to-Silicon Direct Wafer Bonding. *Jpn. J. Appl. Phys.* **2001**, *40*, 4837. [[CrossRef](#)]
16. O'Callaghan, J.; Loi, R.; Mura, E.E.; Roycroft, B.; Trindade, A.J.; Thomas, K.; Gocalinska, A.; Pelucchi, E.; Zhang, J.; Roelkens, G.; et al. Comparison of InGaAs and InAlAs Sacrificial Layers for Release of InP-Based Devices. *Opt. Mater. Express* **2017**, *7*, 4408. [[CrossRef](#)]
17. Menard, E.; Lee, K.J.; Khang, D.-Y.; Nuzzo, R.G.; Rogers, J.A. A Printable Form of Silicon for High Performance Thin Film Transistors on Plastic Substrates. *Appl. Phys. Lett.* **2004**, *84*, 5398–5400. [[CrossRef](#)]
18. Zhang, J.; Muliuk, G.; Juvert, J.; Kumari, S.; Goyvaerts, J.; Haq, B.; Op de Beeck, C.; Kuyken, B.; Morthier, G.; Van Thourhout, D.; et al. III-V-on-Si Photonic Integrated Circuits Realized Using Micro-Transfer-Printing. *APL Photonics* **2019**, *4*, 110803. [[CrossRef](#)]
19. Haq, B.; Haq, B.; Vaskasi, J.R.; Vaskasi, J.R.; Zhang, J.; Zhang, J.; Gocalinska, A.; Pelucchi, E.; Corbett, B.; Roelkens, G.; et al. Micro-Transfer-Printed III-V-on-Silicon C-Band Distributed Feedback Lasers. *Opt. Express OE* **2020**, *28*, 32793–32801. [[CrossRef](#)]
20. Frank-Rotsch, C.; Dropka, N.; Kießling, F.-M.; Rudolph, P. Semiconductor Crystal Growth under the Influence of Magnetic Fields. *Cryst. Res. Technol.* **2020**, *55*, 1900115. [[CrossRef](#)]
21. Giziewicz, K.; Smejkalova, L.; Eichler, S.; Juda, U.; Pietsch, M.; Root, O.; Souptel, D.; Stolze, K.; Weinert, B.; Frank-Rotsch, C. Application of heater magnet module for improved crystal growth of InP. In Proceedings of the 51st Annual Meeting of the German Association of Crystal Growth, Berlin, Germany, 6–8 October 2021.
22. Huber, A.; Linh, N.T. Révélation Métallographique Des Défauts Cristallins Dans InP. *J. Cryst. Growth* **1975**, *29*, 80–84. [[CrossRef](#)]
23. DIN 50454-1:2000-07; Testing of Materials for Semiconductor Technology—Determination of Dislocations in Monocrystals of III-V-Compound Semi-Conductors—Part 1: Gallium Arsenide. Deutsches Institut für Normung: Berlin, Germany, 2000.
24. DIN 50454-1:1994-10; Testing of Materials for Semiconductor Technology—Determination of Dislocations in Monocrystals of III-V-Compound Semi-Conductors—Part 2: Indium Phosphide. Deutsches Institut für Normung: Berlin, Germany, 1994.
25. Pettit, G.D.; Turner, W.J. Refractive Index of InP. *J. Appl. Phys.* **2004**, *36*, 2081. [[CrossRef](#)]
26. Gugushev, C.; Richter, C.; Brützmam, M.; Dadzis, K.; Hirschle, C.; Gesing, T.M.; Schulze, M.; Kwasniewski, A.; Schreuer, J.; Schlom, D.G. Revisiting the Growth of Large (Mg,Zr):SrGa₁₂O₁₉ Single Crystals: Core Formation and Its Impact on Structural Homogeneity Revealed by Correlative X-Ray Imaging. *Cryst. Growth Des.* **2022**, *22*, 2557–2568. [[CrossRef](#)]
27. Stolze, K.; Steglich, P.; Berger, K.; Juda, U.; Martin, J. Verfahren Und Vorrichtung Zum Herstellen Einer Halbleiterstruktur. DE Patent Application 10,2022,100,661.1, 12 January 2022.
28. Kubinyi, M.; Benkö, N.; Grofcsik, A.; Jones, W.J. Determination of the Thickness and Optical Constants of Thin Films from Transmission Spectra. *Thin Solid Films* **1996**, *286*, 164–169. [[CrossRef](#)]
29. Jena, K.C.; Hore, D.K. A Simple Transmission-Based Approach for Determining the Thickness of Transparent Films. *Am. J. Phys.* **2011**, *79*, 256–260. [[CrossRef](#)]
30. Lin, J.; You, T.; Wang, M.; Huang, K.; Zhang, S.; Jia, Q.; Zhou, M.; Yu, W.; Zhou, S.; Wang, X.; et al. Efficient Ion-Slicing of InP Thin Film for Si-Based Hetero-Integration. *Nanotechnology* **2018**, *29*, 504002. [[CrossRef](#)] [[PubMed](#)]
31. Chin, A.K. The Effect of Crystal Defects on Device Performance and Reliability. *J. Cryst. Growth* **1984**, *70*, 582–596. [[CrossRef](#)]
32. Yamaguchi, M.; Yamamoto, A.; Itoh, Y. Effect of Dislocations on the Efficiency of Thin-film GaAs Solar Cells on Si Substrates. *J. Appl. Phys.* **1986**, *59*, 1751–1753. [[CrossRef](#)]
33. Ito, H.; Nakajima, O.; Furuta, T.; Harris, J.S. Influence of Dislocations on the DC Characteristics of AlGaAs/GaAs Heterojunction Bipolar Transistors. *IEEE Electron Device Lett.* **1992**, *13*, 232–234. [[CrossRef](#)]
34. Heidelberger, C.; Fitzgerald, E.A. GaAsP/InGaP HBTs Grown Epitaxially on Si Substrates: Effect of Dislocation Density on DC Current Gain. *J. Appl. Phys.* **2018**, *123*, 161532. [[CrossRef](#)]
35. Beam, E.A.; Temkin, H.; Mahajan, S. Influence of Dislocation Density on I-V Characteristics of InP Photodiodes. *Semicond. Sci. Technol.* **1992**, *7*, A229–A232. [[CrossRef](#)]
36. Jung, D.; Herrick, R.; Norman, J.; Turnlund, K.; Jan, C.; Feng, K.; Gossard, A.C.; Bowers, J.E. Impact of Threading Dislocation Density on the Lifetime of InAs Quantum Dot Lasers on Si. *Appl. Phys. Lett.* **2018**, *112*, 153507. [[CrossRef](#)]

37. Cocito, M.; Franzosi, P.; Salviati, G.; Taiariol, F. Cathodoluminescence Study of Defects in III-V Substrates and Structures. *Scanning Electron Microsc.* **1985**, *1986*, 1299–1310.
38. Adachi, S. Optical dispersion relations for GaP, GaAs, GaSb, InP, InAs, InSb, $\text{Al}_x\text{Ga}_{1-x}\text{As}$, and $\text{In}_{1-x}\text{Ga}_x\text{As}_y\text{P}_{1-y}$. *J. Appl. Phys.* **1989**, *66*, 6030–6040. [[CrossRef](#)]
39. Byrnes, S.J. Multilayer optical calculations. *arXiv* **2016**, arXiv:1603.02720. [[CrossRef](#)]

Disclaimer/Publisher's Note: The statements, opinions and data contained in all publications are solely those of the individual author(s) and contributor(s) and not of MDPI and/or the editor(s). MDPI and/or the editor(s) disclaim responsibility for any injury to people or property resulting from any ideas, methods, instructions or products referred to in the content.